ACS OMEGA

http://pubs.acs.org/journal/acsodf

Article

Characteristics of a Cavitating Spoiler Mixing Device and Its Performance in a Foam Dust Suppression System

Husheng Yang, Xiaolong Zhu,* Ruixia Hu, Kang Zhang, Chaohang Xu, Qingguo Wang, and Hetang Wang*

Cite This: *ACS Omega* 2022, 7, 29886−29900

Read Online

ACCESS | Metrics & More | Article Recommendations | Supporting Information

ABSTRACT: The unsteady foaming-agent mixing ratio in traditional foam-dust-suppression technology limited the dust suppression efficiency. Recent studies proved that the steady mixing ratio could be guaranteed by keeping the jet pumps or Venturis working under cavitation conditions, but the pressure loss of the current devices was over 50%. To decrease the pressure loss under cavitation conditions, we proposed a new mixing device by introducing a spoiler in the Venturi structure. Through computational fluid dynamics (CFD) simulation, the spoiler structure influence on the downstream flow field and the cavitation cloud structure, which affected the total pressure loss of the device, were revealed. For structure optimization, the effect of the other geometric parameters, including the throat length and divergent angle, on the pressure loss was also studied. The proposed device enhanced the cavitation on the suction tube side of the throat; meanwhile, the cavitation in other parts of the device was avoided. Therefore, the cavitation zone in the proposed device was much smaller than that in current devices, and the pressure loss was reduced significantly. When the flow ratio was 0.5−1%, the critical pressure ratio of the proposed mixing device was 0.71−0.68, which indicated that the pressure loss was only 29%−32%. The laboratory experiment verified that when the proposed device worked under cavitation conditions, the accurate and steady mixing ratio was guaranteed. The field experiment indicated that due to the reduced pressure loss of the proposed device, the required water inlet pressure decreased to 0.29 MPa, and the dust suppression rate increased dramatically. This study was of important value in manipulating cavitation cloud structure using a spoiler, clarifying the influence of the cavitation cloud structure on the liquid mixing performance and expanding the application field of the cavitating mixing method.

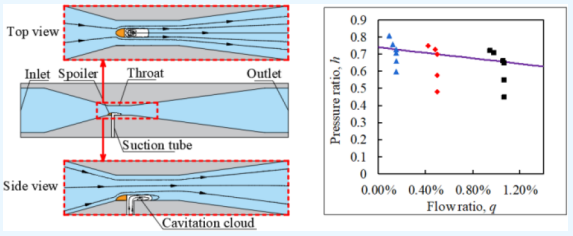

1. INTRODUCTION

With the extension of mechanized excavation technology and mechanized mining technology, dust contamination was getting worse in coal mines. Explosion and pneumoconiosis were the main safety problems caused by mine dust. In China, 58.3% of major safety accidents (more than 100 deaths) in coal mines were related to coal dust explosions.[1] In the United States, at least 476 workers in the Hawk's Nest Tunnel disaster were diagnosed with silicosis.[2] In recent years, new cases of pneumoconiosis were continuously reported in Australia and Britain.[3,4] In China, the number of pneumoconiosis patients was steadily growing,[5,6] and most patients worked at the tunneling working face.[7]

Foam was an effective dust suppression method at belt transfer points and in heading faces of coal mines because of its large wettability, adhesion, and volume.[8−10] Jet pumps were commonly used as automatic foaming-agent mixing devices in foaming systems because of their high reliability, intrinsic safety, low cost, and small volume.[11−14] However, during the field dust-suppression practice, the cutting head movement and the nozzle blocking often resulted in pressure fluctuation downstream of the mixing device, which led to foaming-agent waste, unstable foam quality, and low dust-suppression rate.[15]

To stabilize the foaming-agent mixing ratio, Lu et al. took advantage of the cavitation effect in the jet pump.[16] When the jet pump worked under cavitation conditions, the static pressure in the vapor-occupied zone remained at the water-saturated vapor pressure (highly vacuumed). As a result, both the flow rate and pressure upstream of the vapor-occupied zone remained constant and independent of the downstream pressure.[15,17,18] The critical pressure ratio (the ratio of the device's absolute outlet pressure to the absolute inlet pressure at the critical cavitation point, CPR) reflected the smallest pressure loss necessary to maintain the cavitation conditions. The larger was the value of the CPR, the smaller was the pressure loss at the critical point of the cavitation. The CPR of the mixing device proposed by Lu et al. was as low as 0.3−0.5 when the flow ratio was below 1%.[13,16,17,19] As a result, high inlet-water pressure was required, and the foam spray distance

Received: May 6, 2022
Accepted: August 11, 2022
Published: August 22, 2022

was short when the cavitating mixing device was installed. The large pressure loss was one of the main reasons that hindered the foam-dust-suppression technology's application in more places, such as undergroud mining faces and open-pit mines.

The wall friction, turbulent flow, as well as cavitation bubble generation and collapse resulted in the conversion of mechanical energy into thermal energy, which led to pressure loss in the mixing device. Long indicated that cavitation was easily promoted when the low-static-pressure zone overlapped with the high-turbulence zone, and the cavitation process often caused the most pressure loss in a jet pump.[20] Compared with jet pumps, Venturis had no abrupt cross-sectional area change between the convergent part and the throat, and so the turbulence and cavitation intensity in the throat of Venturis were lower than those in jet pumps with similar geometric parameters. Therefore, the CPR of a Venturi without liquid suction could be as high as 0.7−0.8,[21] which was much higher than those of the current jet pumps. On the basis of the Venturi structure, Zhu et al. optimized the structure of the cavitating mixing device. The CPR of their device increased to 0.6 when the mixing ratio was below 1%.[13,16,17,19] On the one hand, to guarantee a steady and accurate agent mixing ratio, the cavitation cloud must steadily cover the suction tube exit to keep the local pressure at the saturated water vapor pressure. On the other hand, the smaller was the total cavitation cloud volume in the device, the less was the pressure loss. In summary, steadily covering the suction tube exit zone with the smallest cavitation cloud volume was the key to simultaneously realizing an accurate mixing ratio and small pressure loss.

To further reduce pressure loss and to guarantee a steady suction flow rate of the cavitating mixing device, we introduced a spoiler into the traditional Venturi structure. Hence, we termed the proposed device as a "spoiler mixing device". The small-sized spoiler was set at the throat inlet, and the suction tube exit was set on the downstream side of the spoiler. After the water had run through the convergent part of the Venturi, the flow velocity increased dramatically and the static pressure decreased significantly. When the flow passed the spoiler, the turbulence was enhanced downstream of the spoiler. Cavitation could be easily promoted because of the low static pressure combined with the enhanced turbulence downstream of the spoiler. Because of the small size of the spoiler, the initial cavitation zone in the proposed device could be much smaller than that in traditional jet pumps or Venturis. As a result, the smaller cavitation zone may lead to less kinetic-energy dissipation. The pressure loss in the proposed device was expected to be dramatically smaller than that in traditional jet pumps or Venturis. As the suction tube exit was set on the downstream side of the spoiler, the small cavitation zone was expected to keep the suction tube exit in a highly vacuumed state and to guarantee a steady suction flow rate. Under the promotion of the spoiler, a unique non-axisymmetric cavitation cloud may appear in the device, but the flow detail and its effect on device performance were rarely studied. In this work, we studied the geometric parameters' effect on the flow field and cavitation cloud structure through computational fluid dynamics (CFD) simulation. After structure optimization, we tested the operating limit ranges and mixing ratio stability of the manufactured device. Finally, the field-dust-suppression experiments were conducted on the heading faces of coal mines to evaluate the performance of the foam system before and after the traditional mixing device was replaced by the proposed one.

2. THEORETICAL ANALYSIS AND DESIGN

2.1. Primary Flow Rate. The structure of the traditional jet pump is shown in Figure 1(a). The convergent part

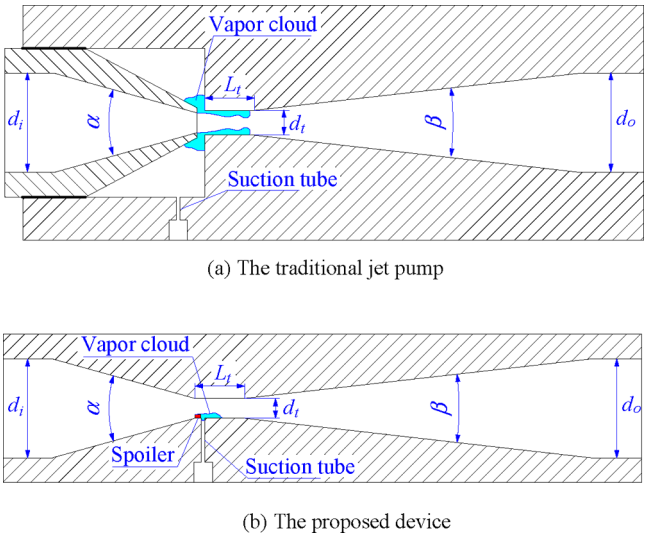

Figure 1. Structure comparison between the traditional jet pump and the proposed device.

accelerated the flow, and so the dynamic pressure was high and the static pressure was low at the contraction section exit. Because there was an abrupt area change between the nozzle exit and the throat inlet, the initial cavitation occurred at the contraction section exit. Assuming a one-dimensional isentropic flow in the contraction section, the flow between the contraction section inlet (cross section 1-1) and the contraction section exit (cross-section 2-2) followed Bernoulli's equation:[17,22]

$$p_i + \frac{1}{2}\rho_l v_i^2 = p_{c,e} + \frac{1}{2}\rho_l v_{c,e}^2 + \xi_1 \frac{1}{2}\rho_l v_{c,e}^2 \quad (1)$$

where p_i and $p_{c,e}$ were the axis center static pressures at section 1-1 and section 2-2, v_i and $v_{c,e}$ were the axis center velocity at section 1-1 and section 2-2, ρ_l was the density of the primary flow, and ξ_1 was the on-way resistance coefficient through the contraction section.

When the working liquid flowed through the contraction section, $v_i \ll v_{c,e}$, the primary mass flow rate m_p was approximately expressed as[19]

$$m_p \approx \sqrt{\frac{1}{1+\xi_1}} \times S_{c,e} \times \sqrt{2\rho_l} \times \sqrt{p_i - p_n} \quad (2)$$

where m_p was the mass flow rate of the primary flow and $S_{c,e}$ was the cross-sectional area of the contraction section exit. Under cavitation conditions, the value of $p_{c,e}$ approximately equaled the saturated vapor pressure of water, P_v (P_v = −97.7 kPa, 20 °C),[22] and so eq 2 could be transformed into

$$m_p \approx \sqrt{\frac{1}{1+\xi_1}} \times S_{c,e} \times \sqrt{2\rho_l} \times \sqrt{p_i - p_v} \quad (3)$$

Neglecting the energy loss along the contraction section, we expressed the theoretical primary flow rate, $m_{p,th}$, as

$$m_{p,th} \approx S_{c,e} \times \sqrt{2\rho_l} \times \sqrt{p_i - p_v} \quad (4)$$

https://doi.org/10.1021/acsomega.2c02814
ACS Omega 2022, 7, 29886−29900

C_d was the discharge coefficient that compensates for the difference between the theoretical primary flow rate and the actual flow rate.[23−25] Hence,

$$m_w = C_d \times S_{c,e} \times \sqrt{2\rho_l} \times \sqrt{P_i - P_v} \quad (5)$$

From eq 5, we could conclude that $S_{c,e}$ was the key geometric parameter that determined the relationship between p_i and m_w. For the proposed Venturi with the spoiler, as shown in Figure 1(b), the maximal velocity and the minimal static pressure occurred where the spoiler exited because the smallest cross-sectional area was reached there. Therefore, the relationship between p_i and m_w for the proposed device was

$$m_w = C_d \times (S_{c,e} - S_s) \times \sqrt{2\rho_l} \times \sqrt{P_i - P_v} \quad (6)$$

where S_S was the spoiler's projected area on the cross section. For traditional jet pumps, the value of C_d was mainly determined by ξ_1; a previous study indicated that $C_d > 0.95$ for traditional jet pumps.[15,26] Since the spoiler led to additional energy loss, the value of C_d was also affected by the spoiler's shape and size in the proposed device. Its value for the proposed device might be different from that for traditional jet pumps.

2.2. Critical Pressure Ratio. The pressure ratio, h, reflected the total pressure loss in the mixing device, which was defined as the absolute pressure ratio between the outlet and the inlet of the device.

$$h = \frac{p_{o,abs}}{p_{i,abs}} \quad (7)$$

where $p_{i,abs}$ and $p_{o,abs}$ were the absolute pressure at the inlet and outlet, respectively, and the subscript *abs* represented the absolute pressure value.

Under normal conditions, both the primary flow rate and the suction flow rate increased with the drop of h. When h decreased below the critical value, h_{cr}, the device turned into cavitation conditions. Under cavitation conditions, the static pressure in the throat cross section remained at the water saturated-vapor pressure, and so both the primary flow rate and the suction flow rate remained constant with the further decrease in h.[20,26] Therefore, the critical pressure ratio, h_{cr}, reflected the total pressure loss at the critical point between the normal conditions and cavitation conditions. The total pressure loss at the critical point was the minimal pressure loss for maintaining the cavitation conditions, which was due to the on-way resistance, turbulence dissipation, cavitation process, and liquid suction. The less was the pressure loss, the higher was the value of h_{cr}. The previous study indicated that when the geometric parameters were determined, the relationship between h_{cr} and the critical flow ratio (the ratio of the suction flow rate to the primary flow rate at the critical point of cavitation, q_{cr}) was self-similar.[20,26] Therefore, the h_{cr}−q_{cr} curve was commonly used to describe the cavitation working range and the pressure loss of a certain cavitating mixing device.[15,18]

2.3. Design of the Cavitating Mixing Device with Spoiler. Because there was an abrupt area change between the nozzle exit and the throat inlet, the turbulence was large in the water jet boundary, as shown in Figure 1(a). As a result, the static pressure in the jet boundary was lower than that in the central part of the cross section. The cavitation occurred when the local static pressure was close to the saturated vapor pressure of water (−97.7 kPa when the temperature was 20 °C).[22] Therefore, the vapor bubbles appeared near the internal wall of the throat at the initial cavitation stage.[18,21] The vapor bubbles expanded to the jet central and downstream at the intensive cavitation stage. To maintain an accurate suction flow rate, it was necessary to keep the cavitation zone at the suction tube outlet, but the bubbles in other zones led to unnecessary additional energy loss. Therefore, we introduced the spoiler in the Venturi to strengthen the cavitation near the suction tube exit and avoid the cavitation in other zones, as shown in Figure 1(b). When the water flowed over the spoiler, strong turbulence occurred in the tail flow, inducing the cavitation. The spoiler size was slightly larger than the suction tube outlet diameter. On the one hand, the cavitation zone could fully cover the suction tube outlet. On the other hand, redundant energy loss was avoided. There was no abrupt area change between the nozzle exit and the throat in the Venturi, and so the turbulence was reduced near the throat wall. Four types of spoiler structures were designed for CFD simulation, as shown in Figure 2(a)−(d). The ratio of the largest height to the

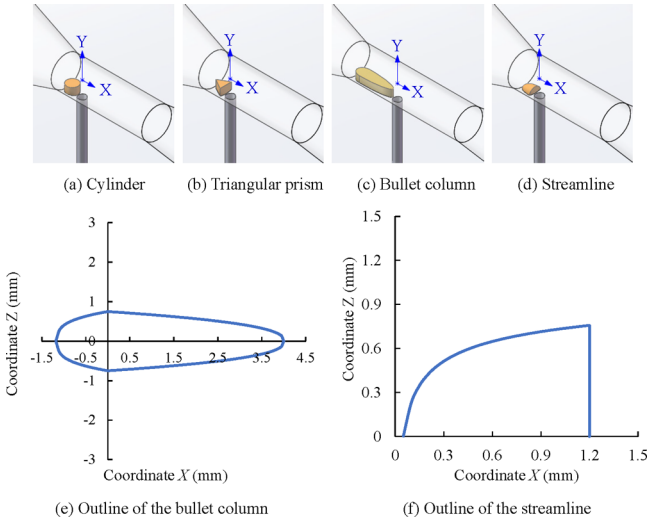

Figure 2. Spoiler structure.

largest width of the spoilers was 1:1.5. Assuming $S_s = 1.5$ mm^2, the outline of the bullet column on cross section X−Z is shown in Figure 2(e) and described by eq 8. The outline of the streamlined spoiler is shown in Figure 2(f) and described by eq 9. After the blue curve in Figure 2(f) was rotated 180° around the X coordinate, a three-dimensional geometry formed. After this geometry was stretched 4/3 times on the Y direction, the streamlined spoiler body was formed.

Equations of the bullet column outline:

$$\begin{cases} z = \pm 0.75 \times \left(\dfrac{4 + 3.5x}{4}\right)^{0.3}, & -1.18 \le x \le 0 \\ z = \pm 0.75 \times \left(\dfrac{4 - x}{4}\right)^{0.4}, & 0 < x \le 4 \end{cases} \quad (8)$$

Equations of the streamlined spoiler outline:

$$\begin{cases} z = 1.23 - 0.5x^{-0.3}, & 0.05 \le x \le 1.2 \\ x = 1.2, & 0 \le z \le 0.75 \end{cases} \quad (9)$$

Because the pipes with an internal diameter of 19 mm were widely used to supply the high-pressure water in coal mines,

https://doi.org/10.1021/acsomega.2c02814
ACS Omega 2022, 7, 29886−29900

the inlet and outlet diameters of the proposed mixing device were set at 19 mm. Previous studies indicated that the resistance loss along the contraction section reached the lowest value when the convergent angle was close to 30°;[21,23] hence, the convergent angle α was set at 31° for the proposed devices. In previous studies,[21] the initial cavitation bubbles appeared at the diffuser inlet when the divergent angle β was higher than 12.5° because the divergent structure induced turbulence and shedding cavitation. Therefore, setting a smaller divergent angle may release the cavitation at the diffuser inlet and reduce the energy loss. To analyze the effect of β on the device performance, it was set at 3°, 5°, 7°, 9°, 11°, 13°, and 15°. In the field-dust-suppression practice using foam, the primary water flow rate was between 2.0 and 3.5 m^3/h, and the water inlet pressure was between 1.0 and 3.0 MPa.[15,16] According to eq 6 and assuming $C_d = 1$, we set $S_{c,e} - S_s$ at 12.56 mm^2. S_s was set at 0.5, 1, 1.5, 2, 2.5, 3, and 3.5 mm^2, respectively, to analyze the spoiler size effect on the device performance. Accordingly, $S_{c,e}$ was set at 13.06, 13.56, 14.06, 14.56, 15.06, 15.56, and 16.06 mm^2, respectively. The dimensionless spoiler size, f_n, was defined as the area ratio of S_s to $S_{c,e} - S_s$. The f_n values were 0.04, 0.07, 0.11, 0.14, 0.17, 0.19, and 0.22, respectively. The throat length, L_t, was set at 5, 10, 15, 20, 25, and 30 mm to analyze its effect on the device performance. The dimensionless throat length, l_t, was defined as the ratio of the throat length, L_t, to the throat diameter, d_t. When f_n was 0.04, the values of l_t were 1.23, 2.45, 3.68, 4.90, 6.13, and 7.35, respectively. The spoiler was set at the inlet of the throat, and the suction tube exit was set closely downstream of the spoiler.

3. METHODS AND MATERIALS

3.1. CFD Model Setup. Because it is challenging to manufacture the proposed devices through the traditional machining method, the devices for the experiment were manufactured through 3D printing technology. Because of the high internal surface roughness, the cavitation zone structure could not be clearly observed in the 3D-printed devices even if the transparent material was applied. Therefore, CFD was applied to study the flow detail in the proposed devices. Yang[25] and Zhu[26] used ANSYS FLUENT to study the cavitation phenomenon in the jet pumps, and the CFD result agreed with their experimental data quite well. Therefore, we applied ANSYS FLUENT in the present work to study the proposed devices, and most of the settings followed the previous studies.

3.1.1. Governing Equations and Key Models. The governing equations and key models for the CFD included continuity equations, momentum equations, turbulence models, and cavitation models. Following the previous studies, the Realizable k-ε model was selected as the turbulence model, which was included in the Reynolds-averaged Navier−Stokes (RANS) models.[27−29] The mixture model was used to solve the water (liquid phase)−vapor (gas phase) boundary, and the Zwart−Gerber−Belamri model was applied to simplify the cavitation process.[24] The details of the above equations were demonstrated in ref 26. The basic assumptions of the above models were as follows.

(a) The cavity cloud consisted of spherical vapor bubbles with the same diameter.
(b) The liquid was incompressible.
(c) The relative velocity between the liquid and vapor bubbles was 0.
(d) Water liquid and vapor had the same pressure.
(e) Temperature was constant at 20 °C.

3.1.2. Meshing of the CFD Models. For all the CFD models, the contraction section exit center was set at the coordinate system origin. The primary flow entered the devices along the positive X-axis direction, and the suction flow entered along the positive Y-axis direction. To obtain accurate results, the hexahedron cells were applied in the suction tube, contraction part, and divergent part of the devices. Because the spoiler made the throat structure complex, the tetrahedral cells were applied to the throat.

3.1.3. Boundary Conditions. The primary liquid inlet, the suction liquid inlet, and the flow outlet were set as pressure boundaries. For all the CFD cases, the primary inlet pressure, p_i, was maintained at 1000 kPa. The suction liquid pressure, p_s, was set at 0, −50, −70, and −90 kPa to control the suction flow rate, which was equivalent to setting the open degree for valve 1 in Figure 3. After p_i and p_s were set, we performed a series of simulation calculations at a different outlet pressure p_o. Because the 3D printer's accuracy was 0.1 mm, the manufactured devices had large internal-wall roughness. Therefore, in FLUENT, the wall-roughness height was set at 0.1 mm, and the roughness constant was set at 1, which was higher than that in the former studies.[26]

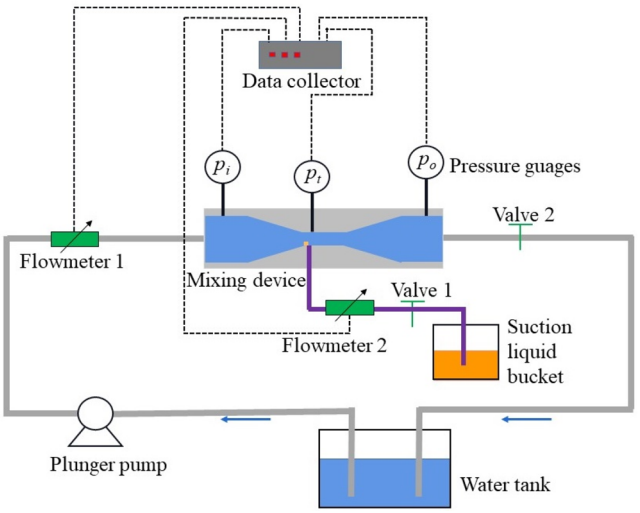

Figure 3. Test system of the proposed mixing device

3.1.4. Solution Setting. Under cavitation conditions, gas and liquid interactions made the flow unstable. Therefore, the unsteady solver was selected. For accurate results, the double-precision method was selected in the calculation process, and the pressure−velocity coupling method was selected for discretization.[28,29] The discretization methods for the governing equations are shown in Table S1 (Supporting Information).[25,26,30] The iteration time step was set at 1×10^{-5} s. The residual error limit of the monitoring parameter was set at 1×10^{-5}. The primary mass flow rate, m_p, and the suction mass flow rate, m_s, were monitored. When the residual errors of all the key parameters were less than 1×10^{-5}, the monitored data became independent of the rise of iteration times. We then considered the result as converged.

3.1.5. Verification of Grid Number Independence. Before the simulation of all the prototypes, the device with the streamlined spoiler was selected to conduct the verification of mesh size independence. The details are provided in the

https://doi.org/10.1021/acsomega.2c02814
ACS Omega 2022, 7, 29886−29900

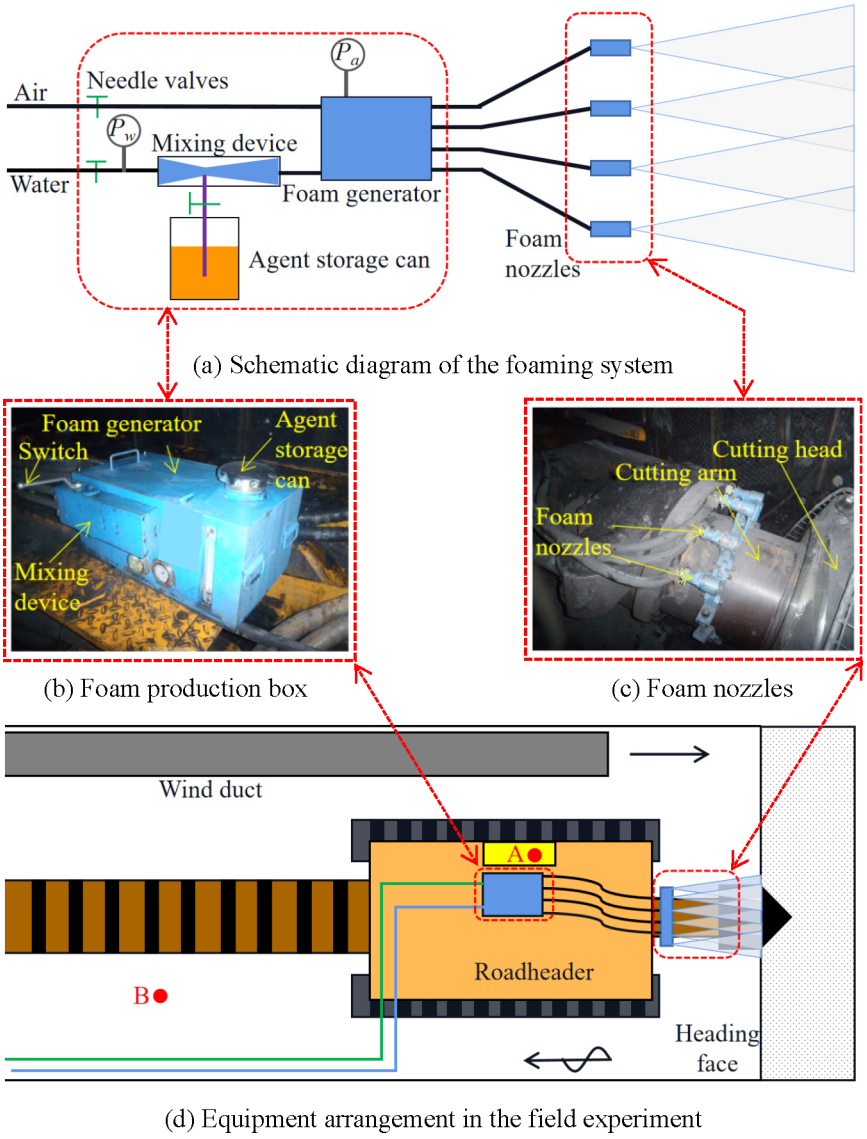

Figure 4. Foam system arrangement in the field experiment.

Supporting Information. As shown in Table S2, the grid number was set at three levels (40,000−50,000, 60,000−70,000, and 90,000−100,000). The mesh quality checking result showed that the minimum orthogonal quality of all the models was above 0.27, and the maximum aspect ratio of all the models was below 12.6 when the grid number was above 40,000. As shown in Figure S1 (Supporting Information), when the grid number was above 60,000, the CFD results of static pressure, velocity magnitude, turbulent intensity, and vapor volume hardly changed with the grid number. The results were accurate enough. Therefore, the grid number of all the models in the present work was set between 60,000 and 70,000.

3.2. Laboratory Experiment Setup. The experimental system is shown in Figure 3. It consisted of the proposed device, water tank, suction liquid bucket, plunger pump, flow meters, pressure gauges, regulating valves, and data acquisition system.

The working liquid and suction liquid were from the water tank and the suction liquid bucket, respectively. The plunger pump drove the primary flow. The primary volume flow rate, Q_p, was regulated by the inbuilt frequency converter, and it was measured by flowmeter 1 (the measurement range was 0.2−6.0 m^3/h, and the precision was 0.50%). The suction volume flow rate, Q_s, was controlled by valve 1, and it was measured by flowmeter 2 (the measurement range was 1−40 L/h, and the precision was 0.50%). Valve 2 set the outlet pressure, p_o. Three pressure sensors were installed to measure the static pressure at the device inlet, p_i, throat, p_t, and device outlet, p_o. The measurement range of the pressure gauges p_i and p_o was 0−2500 kPa, and that of the pressure gauge p_t was −100−100 kPa. The precision of both pressure gauges was 0.25%. The real-time tested data were recorded in the data recorder BK-0896K at a 1.0 Hz sampling rate. The environmental temperature throughout the experiment was constant at 20 °C.

The experimental steps to study the operating limit range were as follows:

(1) Assembly of the experimental test system according to Figure 3. Since the air leakage influenced the cavitation performance dramatically, we applied sealing tape and gasket rings to ensure airtightness at each connection.

https://doi.org/10.1021/acsomega.2c02814
ACS Omega 2022, 7, 29886−29900

Table 1. Basic Conditions of the Field Experiment Locations

Location	Water pressure (MPa)	Compressed air pressure (MPa)	Wind flow rate (m^3/h)	Cross-sectional area of the roadway (m^2)	Roadheader type	Tunneling speed (m/day)
1307 air roadway of Zhaoxian Coal Mine	1	0.4	460−485	16.2	EBZ132	4.3
9102 track roadway of Wangzhuang Coal Mine	2.5	0.4	422−501	16.7	EBZ135	4.8
3109 machine roadway of Zouzhuang Coal Mine	0.29	0.3	523−575	15.3	EBZ120	3.8

(2) The procedure for an experiment cycle was as follows: We fully opened valve 2 and started data collection. We switched on the plunger pump and set m_w at 0.54 kg/s by adjusting the frequency controller. Under this condition, valve 2 is fully open, and so severe cavitation occurs in the device. We then set the critical flow ratio, q_{cr}, at 0.15%, 0.5%, and 1% by adjusting valve 1's open degree in each experiment cycle. Next, we increased p_o by slowly closing valve 2. During the rising of p_o, we continuously recorded the pressure data. When the cavitation noise decreased dramatically, we slowed down the adjustment of valve 2 and decreased the pressure recording interval because the pressure ratio was approaching the critical point. When p_o started to rise with p_i, the device passed the critical point and turned into the normal condition. We then slowly opened valve 2 while recording pressure data until valve 2 was fully open. We then switched off the plunger pump.

The experimental steps to study the primary flow rate were as follows:

(1) We assembled the experimental test system according to Figure 3. We fully opened valve 2 to keep p_o at a low value. We set the open degree of valve 1 at 10%.

(2) We switched on the plunger pump and set p_i at 0.35, 0.4, 0.45, 0.5, 0.55, and 0.6 MPa by adjusting the frequency controller. To make sure the device was under cavitation conditions, the cavitation noise should be loud and clear. We recorded the primary flow rate, Q_m, at different values of p_i. We then turned off the plunger pump.

3.3. Field Experiment Setup. To compare the performance of the foam dust suppression system before and after changing the mixing device, a field experiment was conducted. Figure 4 shows the schematic diagram of the foaming system for coal mine dust suppression. When the high-pressure water flowed through the mixing device, the foaming agent was automatically sucked into the device and was dissolved in the water. The foaming agent solution was then mixed with the pressurized air in the foaming generator to produce foam. Finally, the foam was sprayed onto the dust source. The detailed internal structure of the foaming generator and the foam nozzles was explained in ref 15. In the tunneling face, most of the dust was generated by the roadheader's cutting head. The instantaneous total dust concentration often exceeded 1000 mg/m^3 during the cutting process.[15] Therefore, the foam spray nozzles were set around the cutting arm to guarantee that the foam spray continuously covered the cutting area during the movement of the cutting head. To avoid equipment damage caused by dust, water, or collision in the tunneling face, the foaming-agent storage tank, the mixing device, and the foam generator were set in a steel box with a size of 600 mm × 450 mm × 300 mm. It connected with the high-pressure water pipe, compressed air pipe, and foam nozzles through high-pressure rubber hoses. Because the water pressure and air pressure varied in different coal mines, the needle valves were set at the inlets of the water and air to adjust their flow rates in the foaming system. As the roadheader continuously moved forward, the box was installed on the roadheader body next to the driver. Therefore, it could be conveniently turned on and off by the driver.

To estimate the performance of the foam dust suppression system in different conditions, the field dust suppression experiments were conducted in the 1307 air roadway of Zhaoxian Coal Mine, in Linyou Baoji Shanxi, China, the 9102 track roadway of Wangzhuang Coal Mine in Qugu Changzhi Shanxi, China, and the 3109 machine roadway of Zouzhuang Coal Mine in Suixi Huaibei Anhui, China. The conditions of the above roadways are listed in Table 1. Because the water pressures in the 1307 air roadway of Zhaoxian Coal Mine and the 9102 track roadway of Wangzhuang Coal Mine were above 1 MPa, the water pressure upstream of the mixing device, p_w, was set at 0.5 MPa by adjusting the needle valve. The water flow rate was maintained at 1.57 m^3/h. The other parameters, such as the foam agent concentration (0.5%) and the airflow rate (40 m^3/h) in the foam generator, were set at the same value as that for the 3109 machine roadway of Zouzhuang Coal Mine. We found that the foam flow rate reached 36.3 m^3/h and the foam expansion ratio was 23.1. Because the supplied water pressure was as low as 0.29 MPa in the 3109 machine roadway of Zouzhuang Coal Mine, the needle valve upstream of the mixing device was fully open to set the water flow rate at 1.26 m^3/h. By adjusting the needle valve downstream of the air inlet, the airflow rate was accordingly set at 35 m^3/h. The foam agent concentration was set at 0.5%. It was measured that the foam flow rate reached 31.1 m^3/h and the foam expansion ratio was 24.7 under the above operating parameters, which suggested that the proposed foaming system can produce enough foam even though the water inlet pressure was as low as 0.29 MPa. In the current foam system, the traditional jet pump was used as the mixing device. Its CPR was 0.28 when the flow ratio was 0.5%.[19] In the new foam system, the proposed mixing device was installed. Its CPR was expected to be much higher than the current one.

To analyze the dust-suppression effect, the dust concentration with and without dust-suppression methods was measured during the roadheader's cutting process. Tow dust concentration detectors (CCZ-1000) were respectively set at the driver's position (point A) and the wind return side 10 m away from the heading face (point B), as shown in Figure 4(d). In all three roadways, the original dust concentration and the dust concentration with the foam spray were respectively measured. To compare the performance of the foam system before and after using the proposed mixing device, the dust concentration was measured when the foam spray was produced by the current and new systems. In addition, to compare the dust suppression effect between water spray and

https://doi.org/10.1021/acsomega.2c02814
ACS Omega 2022, 7, 29886−29900

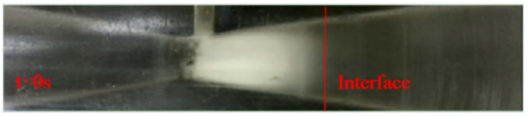

(a) Cavitation cloud distribution in a Venturi (Experiment photograph courtesy of Xiaolong Zhu et al. Copyright 2017) [18]

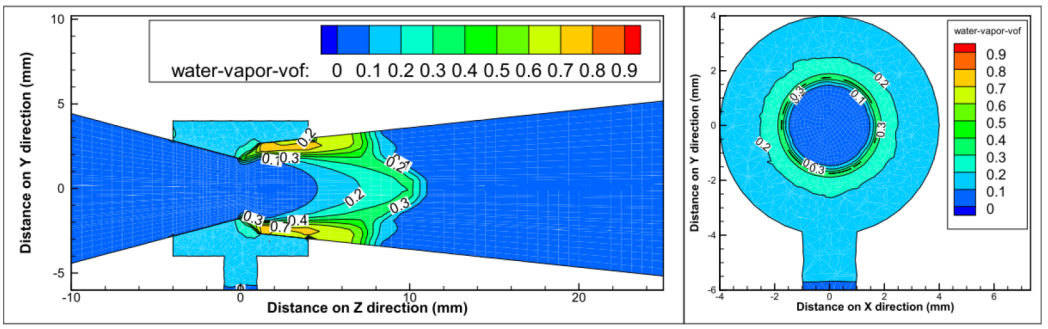

(b) Cavitation cloud distribution in a jet pump (CFD result, photograph courtesy of Xiaolong Zhu et al. Copyright 2018) [26]

Figure 5. Axisymmetric cavitation cloud distribution in traditional Venturis and jet pumps[18,26]

foam, the dust concentration with the water spray on was also tested in the 3109 machine roadway of Zouzhuang Coal Mine. The water pressure was 0.29 MPa and the water flow rate was 2.8 m^3/h for the water spray system. We repeated all the dust concentration measurements five times for each condition, and each measurement took 3 min.

4. RESULTS AND DISCUSSION

4.1. Spoiler Shape Influence on the Cavitation Cloud Structure Formation. To compare different spoilers' effects on the cavitation cloud structure, different spoilers were set in four devices. For a fair comparison, the devices had the same geometric parameters (α = 31°, β = 13°, L_t = 10 mm, f_n = 0.11), except for the spoiler shape. The same boundary conditions were also set (p_i = 1000 kPa, p_o = 450 kPa, Q_s = 0 L/h).

Figure 5 shows the cavitation cloud structures in traditional Venturis and jet pumps. Because the divergent structure and the abrupt change of the flow cross section led to a great velocity gradient near the internal wall of the diffuser inlet, intensive turbulence occurred there.[18,26] As the low static pressure and high turbulence combined at the diffuser inlet, an axisymmetric circled cavitation cloud was promoted. Figure 6(a) shows the cavitation cloud in the proposed devices. Since the spoiler was introduced in the Venturi structure, the cavitation cloud appeared in the downstream flow of the spoiler before any cavitation bubble appeared at the diffuser inlet. This was evidence that the cavitation occurred more easily at the spoiler than at the diffuser inlet. Because the cavitation cloud promoted by the spoiler was non-axisymmetric, if the spoiler structure was well designed, then the cavitation cloud volume downstream of the spoiler could be much smaller than the axisymmetric circled cloud in traditional devices at the initial cavitation stage (Figure 5).

To analyze the cavitation cloud structures under the effects of different spoilers, Figure 6(b) demonstrates the velocity field and turbulent intensity around the spoilers. On the flow incoming side of the cylinder spoiler and the bullet column spoiler, there was a height stage of 1 mm, and the sidewall curvature radius was relatively large, and so the flow turned in three directions (+Z, −Z, and +Y) abruptly. The abrupt direction change caused a great velocity gradient on the spoiler top, and so the cavitation cloud appeared on the top of the cylinder spoiler and the bullet column spoiler (Figure 6(a)). However, the cavitation cloud did not appear on the top of the triangular prism spoiler and the streamlined spoiler. For the triangular prism spoiler, the acute angle of the sidewalls made the flow gradually turn to the +Z and −Z directions, and so the turbulent intensity was low on the top of the spoiler. For the streamlined spoiler, there was no height stage on the incoming side, and so the flow direction changed smoothly along the top and sidewalls of the spoiler. This led to low turbulent intensity on the top of the spoiler.

For the cylinder spoiler and the bullet column spoiler, their cross-sectional area first increased and then gradually decreased when the distance increased in direction +X. When their cross-sectional area started to decrease, the great velocity gradient near the sidewalls caused vortex shedding, and so cavitation clouds appeared along the sidewalls on the downstream side of the spoilers (Figure 6(a)). For the triangular prism spoiler and the streamlined spoiler, there was no gradual cross-sectional area reduction in direction +X. Therefore, no cavitation cloud appeared along the sidewalls, as shown in Figure 6(a).

Because there was a height stage of 1 mm on the incoming side of the cylinder spoiler, bullet column spoiler, and triangular prism spoiler, the velocity component in directions +Z and −Z was relatively large in the downstream flow of the spoilers. The high-velocity flow on the +Z and −Z sides led to low static pressure and high turbulence, and so the cavitation cloud in the downstream flow had a V-shaped structure, as shown in Figure 6(a). The streamlined spoiler did not have a height stage on the incoming side. Therefore, the velocity component in directions +Z and −Z was still small in the

https://doi.org/10.1021/acsomega.2c02814
ACS Omega 2022, 7, 29886−29900

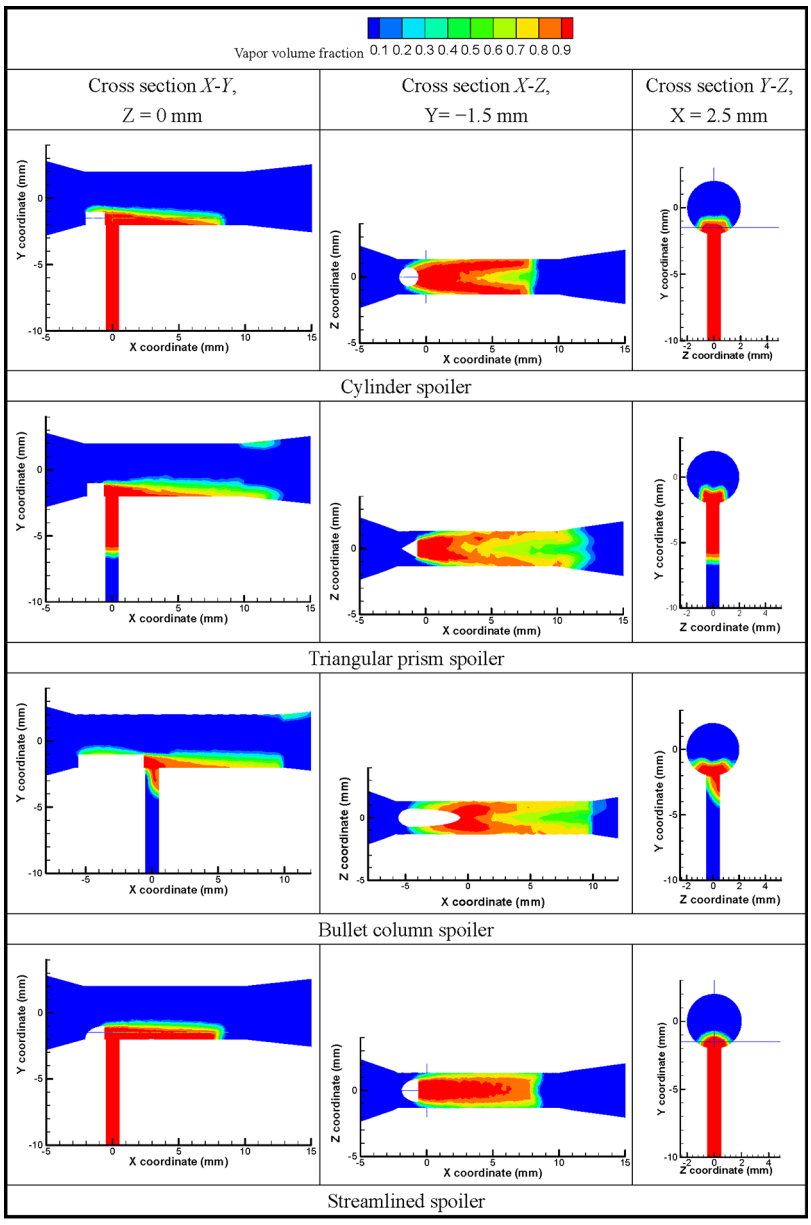

(a) Vapor volume fraction

Figure 6. continued

https://doi.org/10.1021/acsomega.2c02814
ACS Omega 2022, 7, 29886−29900

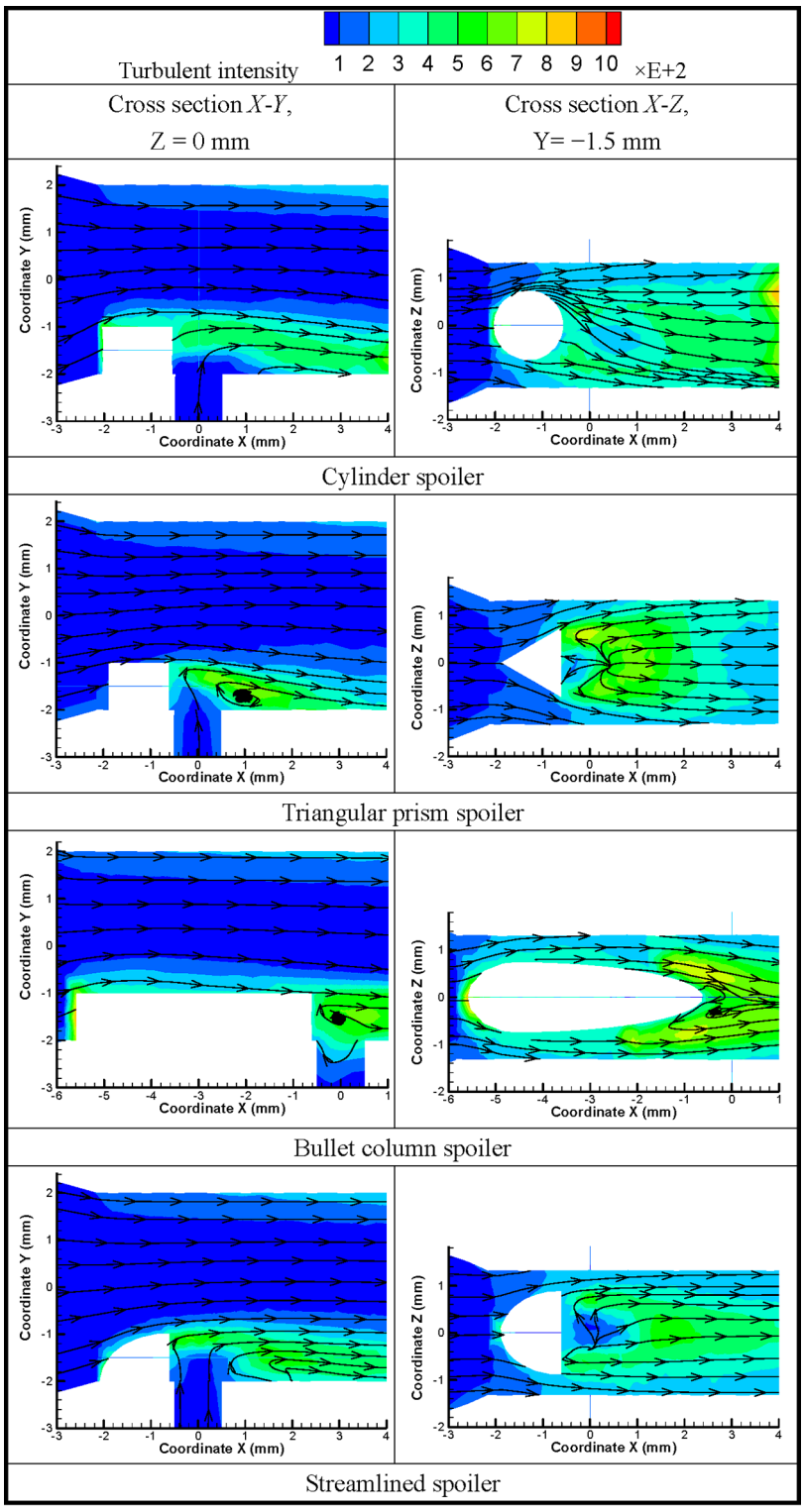

(b) Turbulent dissipation rate

Figure 6. Effect of spoiler shape on the distribution of turbulent intensity, cavitation cloud, and negative pressure (p_i = 1000 kPa, p_o = 450 kPa, Q_s = 0 L/h).

downstream flow of the spoiler. Therefore, the cavitation cloud downstream of the spoiler remained along the central line.

To quantitatively compare the cavitation clouds promoted by different spoilers, the cavitation cloud volume and length were demonstrated in Figure 7. The total vapor volume in different devices is shown in Figure 7(a). When p_o = 400 kPa, the vapor volume in the streamlined spoiler device was the smallest. However, with the rise of p_o, the vapor volume decrease gradient of the streamlined spoiler device was dramatically slower than the other devices. When p_o increased to 525 kPa, only the vapor volume in the streamlined spoiler device was above 5 mm^3, and that in the other devices was

https://doi.org/10.1021/acsomega.2c02814
ACS Omega 2022, 7, 29886−29900

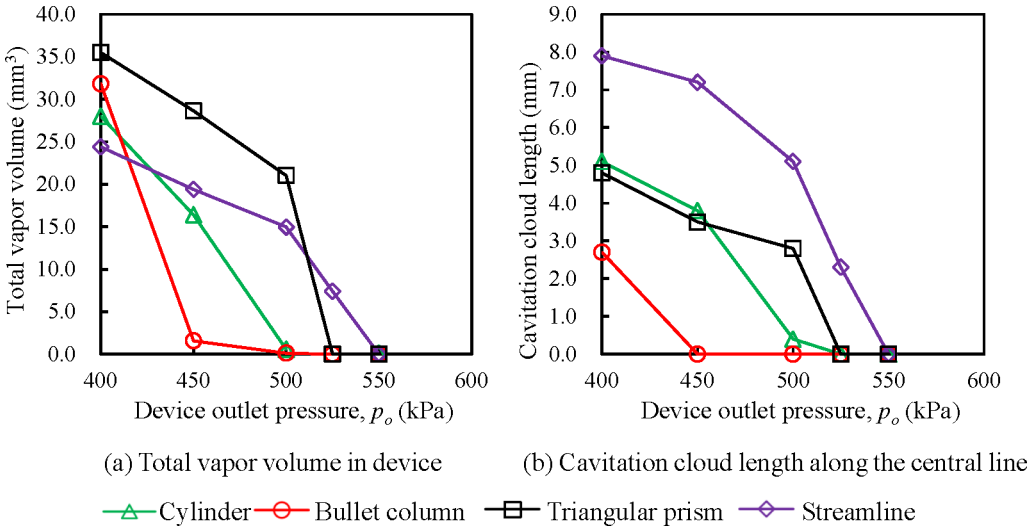

Figure 7. Total cavitation volume and cavitation cloud length of four types of devices (p_i = 1000 kPa).

below 0.1 mm^3. The cavitation cloud length downstream of the spoiler is shown in Figure 7(b). Because the cavitation cloud outline fluctuated with time, we presented the length of the cavitation cloud with a vapor volume fraction above 0.7. This length hardly changed with the iteration time step. Although the total vapor volume in the streamlined spoiler device was not the largest, the cavitation cloud length in it was much longer than that in the other devices. The reason was that only the cavitation cloud downstream of the streamlined spoiler was maintained along the device's central line, while the cavitation clouds downstream of the other spoilers had a V-shaped structure, as shown in Figure 6(a). Because the suction tube was set downstream of the spoiler, only the cavitation cloud downstream of the spoiler helped stabilize the suction flow rate. However, the cavitation clouds on the spoilers' top and along the spoilers' sidewalls were useless in terms of stabilizing the suction flow rate. They just resulted in redundant energy loss. Therefore, the cavitation cloud promoted by the streamlined spoiler had a better structure than that promoted by the other spoilers.

To compare the effect of the spoiler's shape on the critical point between the cavitation and normal conditions, the suction tube exit pressure, p_s, was measured at different device outlet pressures, p_o (p_i was kept at 1000 kPa), as shown in Figure 8. When p_o was below the critical point, the cavitation cloud steadily covered the suction tube exit, and p_s remained close to the water-saturated vapor pressure. When p_o exceeded the critical point, the cavitation cloud could not cover the suction tube exit, and p_s increased with the rise of p_o. Therefore, it was observed that the critical points in Figure 8 were quite close to that in Figure 7(b), where the cavitation cloud length just dropped to 0 mm. In Figure 8, the critical outlet pressure of the device with the streamlined spoiler was 527 kPa, and that of the device with the other spoiler was below 500 kPa. This result confirmed that the streamlined spoiler caused the smallest pressure loss among the four types of spoilers at the critical point between cavitation and normal conditions. Consequently, the device with a streamlined spoiler was the best choice for the proposed mixing device.

4.2. Optimization of the Other Geometric Parameters. Because the CPR directly reflected the minimal pressure loss of the cavitating device, we used the control variable

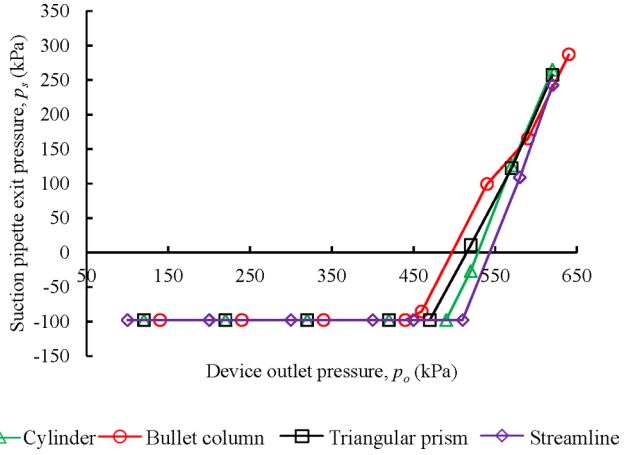

Figure 8. Spoiler shape influence on the turning point of the suction tube inlet pressure (p_i = 1000 kPa, Q_s = 0 L/h).

method to analyze the influence of spoiler size, throat length, and divergent angle on the CPR one by one. The data on p_s were collected by keeping p_i = 1000 kPa and Q_s = 0 L/h and by setting p_o at different values. The critical points of cavitation could then be determined on the basis of p_s–p_o curves, as shown in Figure 8. According to eq 7, the CPR without liquid suction, $h_{cr,0}$, could be calculated.

To study the effect of the spoiler size on $h_{cr,0}$, β was set at 13°, L_t was set at 10 mm, and S_s was set at 0.5, 1, 1.5, 2, 2.5, 3, and 3.5 mm^2. Accordingly, the values of f_n were 0.04, 0.07, 0.11, 0.14, 0.17, 0.19, and 0.22, respectively. $h_{cr,0}$ at different f_n is shown in Figure 9(a). $h_{cr,0}$ decreased from 0.65 to 0.37 when f_n increased from 0.04 to 0.22. This indicated that the larger was the spoiler size, the more energy dissipation was required to remain in the cavitation conditions. Therefore, the smallest size of the spoiler was selected for the structure optimized device (f_n = 0.04, $S_{c,e}$ = 13.06 mm^2, and $d_{c,e}$ = d_t = 4.08 mm).

To study the effect of the throat length on $h_{cr,0}$, β was set at 13°, f_n was set at 0.04, and L_t was set at 5, 10, 15, 20, 15, and 20 mm. Accordingly, the value of l_t was 1.23, 2.45, 3.68, 4.90, 6.13, and 7.35, respectively. $h_{cr,0}$ at different l_t is shown in Figure 9(b). $h_{cr,0}$ increased from 0.61 to 0.65 when l_t increased from 1.23 to 2.45. The reason was that a certain length of the

https://doi.org/10.1021/acsomega.2c02814
ACS Omega 2022, 7, 29886−29900

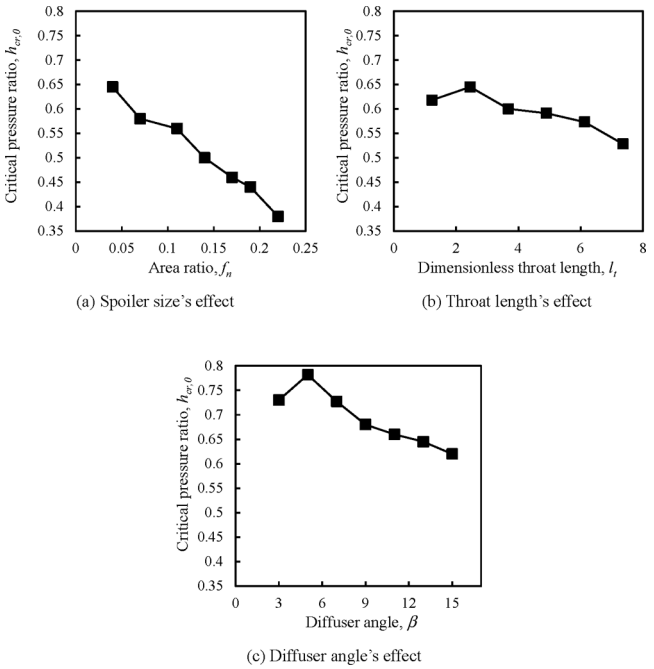

(a) Spoiler size's effect (b) Throat length's effect

(c) Diffuser angle's effect

Figure 9. Geometric parameters' effects on the critical pressure ratio (Q_s = 0 L/h).

throat was needed to keep the spoiler tail flow at high velocity and low static pressure. The low-pressure zone was not long enough when l_t was below 2.45. It was also observed that $h_{cr,0}$ decreased from 0.65 to 0.53 when l_t increased from 2.45 to 7.35. The reason was that the effect of on-way resistance emerged when l_t exceeded 2.45. Because $h_{cr,0}$ reached the largest value when l_t = 2.45, a throat length of 10 mm was selected for the structure optimized device.

As $S_{c,e}$ = 13.06 mm^2, $d_{c,e}$ = d_t = 4.08 mm, and L_t = 10 mm were determined in the above analysis, β was set at 3°, 5°, 7°, 9°, 11°, 13°, and 15° to study its effect on $h_{cr,0}$. As shown in Figure 9(c), when β decreased from 15° to 5°, $h_{cr,0}$ increased from 0.63 to 0.78. This is because the turbulence at the diffuser inlet decreased with the decrease in β, as discussed at the design stage (section 2.3). However, it was observed that $h_{cr,0}$ decreased from 0.78 to 0.73 when β decreased from 5° to 3°. The reason was that increasing diffuser length led to the rise of on-way resistance. Since $h_{cr,0}$ reached its highest value when β = 5°, β of the structure optimized device was set at 5°. It was worth noting that β of the proposed device was much smaller than that of the traditional Venturi proposed by Ghassemi, Ulas, and Abdulaziz (12°−14°).[21−23] The reason was that the initial cavitation in the traditional Venturi occurred at the diffuser inlet, and so β should be large enough to enhance the turbulence there. However, the proposed device relied on the spoiler to promote initial cavitation, rather than the diffuser structure. Therefore, setting β at a smaller value resulted in smaller pressure loss in the diffuser.

In summary, when f_n = 0.04, l_t = 2.45, and β = 5°, the critical pressure ratio reached 0.78 when no liquid suction was involved. This indicated that after the optimization of the geometric parameters, a small pressure loss (below 22%) was realized.

4.3. Laboratory Test Result of the Proposed Mixing Device Performance. *4.3.1. Range of Operating Limits.* On the basis of the CFD result, the mixing device with the optimized structure was fabricated and tested in the experimental system shown in Figure 3. The experimental steps were described in section 3.2. On the basis of the measured p_i and p_o under different conditions, the pressure ratio, h, was calculated according to eq 7. The experiment result was compared with the CFD result in Figure 10(a). The filled and unfilled scatters were, respectively, the experimental and CFD data of the same mixing device. In the experiment, the open degree of valve 2 was respectively set at 40%, 60%, and 80%. In the CFD model, the suction tube inlet pressure was set at 0, −50, −70, and −90 kPa to simulate the different open degrees of valve 2.

As shown in Figure 10(a), when the device worked under cavitation conditions, the flow ratio, q, stayed constant and independent of h. When the device worked under normal conditions, q decreased with the rise of the pressure ratio, h.

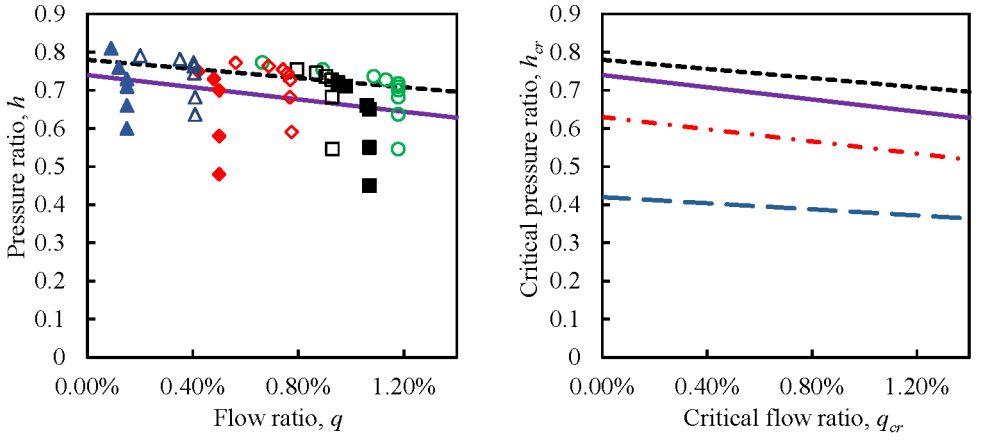

(a) Experiment result compared with CFD (b) Comparison between different devices

Figure 10. Pressure ratio vs flow ratio: (filled blue triangles) valve 2 open degree = 50% in experiment; (filled red diamonds) valve 2 open degree = 30% in experiment; (black boxes) valve 2 open degree = 10% in experiment; (green circles) p_s = 0 kPa in CFD; (open boxes) p_s = −50 kPa in CFD; (open red diamonds) p_s = −70 kPa in CFD; (open blue triangles) p_s = −90 kPa in CFD; (dashed black line) CFD fitting curve of the proposed mixing device; (solid purple line) experimental fitting curve of the proposed mixing device; (dashed red line) experimental fitting curve of device A; (solid blue line) experimental fitting curve of device B.

https://doi.org/10.1021/acsomega.2c02814
ACS Omega 2022, 7, 29886−29900

Table 2. Key Geometric Parameters of the Current Cavitating Mixing Device

Device name	α (deg)	β (deg)	d_i (mm)	d_o (mm)	d_n (mm)	d_t (mm)	L_t (mm)	Reference
B	13.3	14	20	20	4	5	20	Lu[16]
A	12.3	12.3	15	15	4	4	2	Zhu[18]

The critical points between the normal and cavitation conditions were fitted by a curve. The area below the curve was the working range of the cavitation conditions. Generally, the fitting curve of the experimental results agreed well with that of the CFD results. But it was observed that the fitting curve of the experimental data was slightly lower than that of the CFD results. This was due to the machining error of the 3D printer. We cut open the device after the experiment, and we found that the wall roughness was large. Besides, the internal diameters were 0.05−0.16 mm smaller than the designed diameters. If the mixing device was manufactured with better precision, its cavitation working range would be as large as that for the CFD results.

In Figure 10(b), the tested q_{cr}−h_{cr} curve of the proposed device was compared with the current cavitating mixing device proposed by previous scholars. The geometric parameters of the compared devices are demonstrated in Table 2. The fitting curve of the proposed device was dramatically higher than the current devices, indicating that the proposed device had less pressure loss than the present devices to maintain the cavitation conditions. In the foam dust suppression system, the agent concentration was about 0.5%. Because h_{cr} of the proposed device was above 0.7 when q_{cr} = 0.5%, the pressure loss of the proposed device could be lower than 30% if it was installed in the dust-suppression system.

4.3.2. Relationship between the Device Inlet Pressure and the Primary Liquid Flow Rate. For traditional jet pumps and Venturis, the relationship between p_i and Q_m could be described by eq 6, as explained section 2.1. Because the cavitation cloud structure of the proposed device was non-axisymmetric, whether eq 6 was still correct remained to be verified by experiment. Therefore, as described in section 3.2, p_i and Q_m were measured under cavitation conditions. The measured data were compared with the theoretical prediction curve, as shown in Figure 11. The tested data agreed well with the theoretical curve when C_d was set at 0.95. The value of C_d indicated that the energy loss caused by the streamlined spoiler was relatively small. Because eq 6 was still valid for the proposed device, the non-axisymmetric cavitation cloud in the proposed device had the same ability to control the primary flow rate as the axisymmetric cavitation clouds in traditional jet pumps and Venturis. With eq 6 valid, the proposed device could work as a flowmeter without an electric supply when p_i was measured by a pressure gauge. This advantage was of great value when the proposed device was installed in explosion-risk or fire-risk places such as coal mining places.

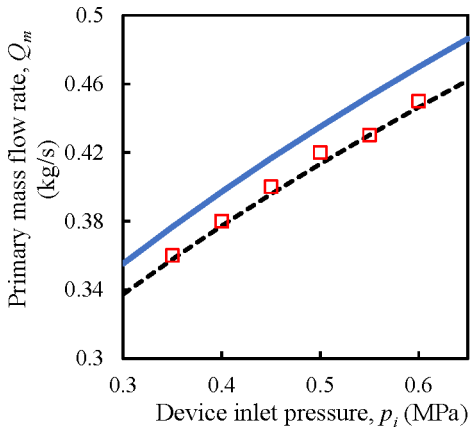

Figure 11. Primary flow rate vs device inlet pressure: (red boxes) tested data; (solid line) theoretical predicted curve when C_d = 1; (dashed line) theoretical predicted curve when C_d = 0.95.

4.3.3. Liquid Suction Stability. To verify the suction flow rate stability of the proposed mixing device, the device outlet pressure was continuously adjusted up and down when the device inlet pressure was set at 900 kPa, and the open degree for valve 2 was set at 30%. The real-time measured p_i, p_o, and Q_s are shown in Figure 12. When the time was between 1600 and 2016 s, the device was under cavitation conditions. It was observed that Q_s remained constant during the variation of p_o. When the time was between 2016 and 2089 s, the pressure ratio, h, exceeded the critical value h_{cr}, and so the device worked under normal conditions. Under this condition, the variation trend of p_i agreed with that of p_o, and the variation trend of Q_s was negative of that of p_o. When the time was between 2089 and 2200 s, h remained near the critical pressure ratio, and Q_s turned back to the steady-state. However, slight fluctuation of Q_s was observed when h was close to h_{cr}. In conclusion, although the cavitation zone structure in the proposed device was non-axisymmetric, the steady suction flow rate was still guaranteed under cavitation conditions. The proposed device was adequate to be an agent mixing device.

4.4. Field Application of the Proposed Device in the Foam-Dust-Suppression System. To show the advantage of the proposed mixing device, the dust-suppression rates before and after the proposed device was applied are compared in Table 3. Generally, the original dust concentration at position B was higher than that at position A because the driver's position was close to the wind duct outlet, and the fresh air diluted the dust concentration there.

In the 1307 air roadway and 9102 track roadway, the water flow rate and the airflow rate were respectively kept at the same value before and after installing the proposed mixing device in the foam system. Because of the large pressure loss (small CPR) in the current mixing device, the pressure fluctuation in the foam generator led to an unstable foaming-agent mixing ratio. In particular, when the cutting head was elevated to cut the roof, foam production and foam spray became unstable, which resulted in the dust escaping. Because the proposed mixing device solved the problem of large pressure loss, the foam spray impact force and the spray stability in the new foam system were much larger than those in the present system. Therefore, the dust-suppression rate of the new foam system was 4.64%−8.95% higher than that of the current foam system, as shown in Table 3.

In the 3109 machine roadway, the current foam system could not work normally because the supplied water pressure was low (0.29 MPa). However, when the proposed mixing device was installed, the new foam system worked normally. Therefore, the dust suppression rate of the new foam system

https://doi.org/10.1021/acsomega.2c02814
ACS Omega 2022, 7, 29886−29900

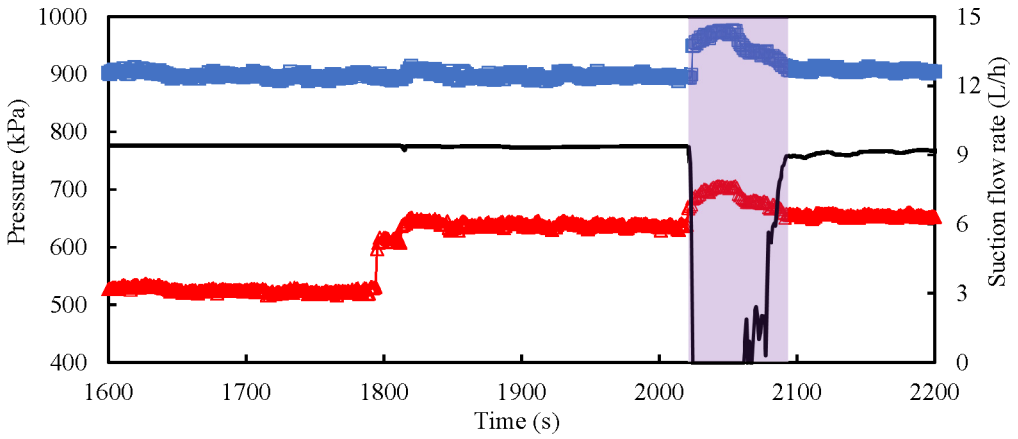

Figure 12. Real-time tested p_i and Q_s with the variation of p_o (valve 2 open degree = 60%): (blue) device inlet pressure, p_i; (red) device outlet pressure, p_o; (solid black line) suction flow rate, Q_s.

Table 3. Measured Dust Concentrations (mg/m^3) and the Dust-Suppression Rates

Location	Repeat number	Total dust	Respirable dust	Total dust	Respirable dust	Total dust	Respirable dust
		Original dust		Current foam system		New foam system	
1307 air roadway, position A	1	815.3	362.5	154.3	70.6	91.6	50
	2	789.3	381.2	169.2	61.3	89.8	49.8
	3	801.1	374.2	157.9	71.1	84.9	50.4
	4	797.4	369.6	163.2	69.6	86.2	46.4
	5	811.6	371.9	158.3	62.1	87.3	52.3
	Average dust suppression rate			80.10%	81.80%	89.05%	86.61%
1307 air roadway, position B	1	989.3	481.2	165.4	77.9	92.7	61.8
	2	1011.6	471.9	176.2	92.4	91.3	63.7
	3	1015.3	462.5	162.9	78.2	117.1	50.2
	4	1001.1	474.2	178.2	86.7	94.1	66.9
	5	997.4	469.6	169.8	89.5	106.3	64.1
	Average dust suppression rate			83.10%	82.10%	90.10%	87.10%
		Original dust		Current foam system		New foam system	
9102 track roadway, position A	1	836.2	402.5	174.8	85.9	103.7	61
	2	841.1	413.2	184.3	81.1	109.8	62.8
	3	821.5	399.2	173.9	76.1	100.4	60.2
	4	844.9	409.8	172.6	85.3	103.4	64.8
	5	831.2	410.3	171.1	78.6	110.2	61.8
	Average dust suppression rate			79.10%	80.10%	87.36%	84.74%
9102 track roadway, position B	1	1132.1	510.2	233.7	102.6	131.8	71.9
	2	1068.8	506.6	231.2	104.2	138.5	76.8
	3	1098.2	502.7	225.8	96.8	131.2	68.3
	4	1143.2	499.8	234.1	102.4	126.3	72.4
	5	1054.6	508.4	229.5	99.5	134.8	69.8
	Average dust suppression rate			79.00%	80.20%	87.95%	85.79%
		Original dust		Water spray		New foam system	
3109 machine roadway, position A	1	856.4	476.3	502.1	286.2	132.4	66.3
	2	866.7	488.2	511.2	291.5	138.9	69.2
	3	887.2	494.3	520.3	302.3	140.7	72.5
	4	890.1	501.2	527.4	310.3	154.7	81.3
	5	876.5	485.5	510.3	312.5	133.3	75.4
	Average dust suppression rate			41.30%	38.50%	84.00%	85.10%
3109 machine roadway, position B	1	1263.3	689.6	756.6	465.4	201.3	102.7
	2	1215.6	653.7	747.5	473.5	205.6	108.4
	3	1156.1	686.2	766.7	486.6	210.3	110.4
	4	1106.7	687.3	770.2	496.4	213.5	122.3
	5	1101.5	675.4	772.3	481.3	218.6	115.6
	Average dust suppression rate			34.70%	29.20%	82.00%	83.50%

was compared with that of the water spray. Because of the poor atomization effect at the low water pressure, only 29.20%−41.30% of the respirable dust was suppressed by the water spray, with a water flow rate of 2.8 m^3/h. Because the foam

https://doi.org/10.1021/acsomega.2c02814
ACS Omega 2022, 7, 29886−29900

(a) Original dust (b) With water spray (c) With foam spray

Figure 13. Photos during the dust concentration measurements.

continuously wetted the cutting head and formed a thick layer at the dust source, 82.00%−85.10% of the respirable dust was suppressed by the foam with the water flow rate of 1.49 m^3/h. Therefore, the proposed mixing device expanded the application field of the foam-dust-suppression method to the locations where the water pressure was lower than 0.3 MPa. A high dust-suppression rate and low water consumption were guaranteed.

The photos during the roadheader cutting process are shown in Figure 13. Because a large amount of dust was diffused in the whole heading face during the cutting process, the visibility was below 2 m when no dust-suppression method was applied, as shown in Figure 13(a). When the water spray was applied, the cutting head was visible, but the escaped dust and the diffused droplets blurred the view, as shown in Figure 13(b). When the foam spray was applied, the view became clear, and it was observed that the white foam layer stayed on the heading face, as shown in Figure 13(c).

5. CONCLUSION

(1) This was the first time that the spoiler was introduced in the cavitating mixing device. The spoiler shape influence on the cavitation cloud structure was explained on the basis of the local velocity field, turbulent intensity distribution, and local pressure distribution. It was found that the cavitation cloud promoted by the streamlined spoiler had the best structure to steadily cover the suction tube exit.

(2) Through the control variable method, the effect of the geometric parameters, including spoiler shape, spoiler size, throat length, and divergent angle, on the cavitation critical point was clarified, and the optimized structure was proposed. When the flow ratio was between 0.5% and 1%, the CPR of the proposed mixing device was between 0.71 and 0.68. This indicated a much wider cavitation working range of the proposed device than the current cavitating mixing devices. It was verified that the non-axisymmetric cavitation cloud that appeared in the proposed device could keep both the suction and primary flow rate steady and independent of the downstream pressure fluctuation. Therefore, accurate and steady liquid mixing was guaranteed. For the proposed device, the relationship between the primary flow rate and inlet pressure could be accurately predicted by eq 6. Therefore, the proposed device could work as a flowmeter without an electric supply when the inlet pressure was measured. This function was of great value when the proposed device was installed in explosion-risk and space-limited places such as coal mines.

(3) The dust-suppression experiment result in the real heading faces indicated that the proposed mixing device was compatible with the foaming system. The accurate mixing of the foaming agent was realized. Because of the reduction of the pressure loss in the mixing device, the foaming system was able to resist large downstream pressure fluctuation, and the foam spray impact force was enhanced. The proposed device even made the foam system work normally when the water inlet pressure was as low as 0.29 MPa. As a result, the new foaming system showed a significant advantage in terms of the dust-suppression rate and application extensiveness.

■ ASSOCIATED CONTENT

Supporting Information

The Supporting Information is available free of charge at https://pubs.acs.org/doi/10.1021/acsomega.2c02814.

CFD discretization methods; grid number independence verification; mesh numbers of different levels; and CFD results comparison under different grid numbers (PDF)

■ AUTHOR INFORMATION

Corresponding Authors

Xiaolong Zhu − *State Key Laboratory of Fire Science, University of Science and Technology of China, Hefei 230026, P.R. China;* orcid.org/0000-0002-7350-2592; Email: cqrczxl@163.com

Hetang Wang − *Key Laboratory of Gas and Fire Control for Coal Mines of Ministry of Education, China University of Mining and Technology, Xuzhou 221116, P.R. China;* Email: wanghetang@cumt.edu.cn

Authors

Husheng Yang − *Key Laboratory of Gas and Fire Control for Coal Mines of Ministry of Education, China University of Mining and Technology, Xuzhou 221116, P.R. China; Shaanxi Blower Group Co. LTD, Xi 'an 710082, P.R. China*

Ruixia Hu − *School of Material Engineering, Shaanxi Polytechnic Institute, Xianyang 712000, P.R. China*

Kang Zhang − *Key Laboratory of Gas and Fire Control for Coal Mines of Ministry of Education, China University of Mining and Technology, Xuzhou 221116, P.R. China*

Chaohang Xu − *School of Safety Science and Emergency Management, Wuhan University of Technology, Wuhan 430070, P.R. China;* orcid.org/0000-0002-0373-9674

Qingguo Wang − *College of Safety Science and Engineering, Nanjing Tech University, Nanjing, Jiangsu 211816, P.R. China;* orcid.org/0000-0001-6066-0260

Complete contact information is available at:

https://doi.org/10.1021/acsomega.2c02814
ACS Omega 2022, 7, 29886−29900

https://pubs.acs.org/10.1021/acsomega.2c02814

Notes

The authors declare no competing financial interest.

■ ACKNOWLEDGMENTS

This work has been funded by the Fundamental Research Funds for the Central Universities (2020CXNL10), the University Synergy Innovation Program of Anhui Province (GXXT-2020-059), and the National Natural Science Foundation of China (51904158).

■ REFERENCES

(1) Li, S.; Zhou, G.; Wang, Y.; Jing, B.; Qu, Y. Synthesis and characteristics of fire extinguishing gel with high water absorption for coal mines. *Process Saf. Environ. Prot.* **2019**, *125*, 207−218.
(2) Spangler, P. *The Hawks Nest Tunnel: An unabridged history*; Wythe-North Publishing: 2008.
(3) Castranova, V.; Vallyathan, V. Silicosis and coal workers' pneumoconiosis. *Environ. Health Perspect.* **2000**, *108*, 675−684.
(4) Kirby, T. Australia reports on audit of silicosis for stonecutters. *Lancet.* **2019**, *393* (10174), 861.
(5) Chen, H.; Feng, Q.; Long, R. Y.; Qi, H. Focusing on coal miners' occupational disease issues: A comparative analysis between China and the United States. *Saf. Sci.* **2013**, *51* (1), 217−222.
(6) Wang, Q. G.; Wang, D. M.; Wang, H. T.; Han, F. W.; Zhu, X. L.; Tang, Y.; Si, W. B. Optimization and implementation of a foam system to suppress dust in coal mine excavation face. *Process Saf. Environ. Prot.* **2015**, *96*, 184−190.
(7) Wang, H.; Wang, D.; Ren, W.; Lu, X.; Han, F.; Zhang, Y. Application of foam to suppress rock dust in a large cross-section rock roadway driven with roadheader. *Adv. Powder Technol.* **2013**, *24* (1), 257−262.
(8) Wei, X.; Du, Y.; Wang, D. Experimental investigation on the dilatational interfacial rheology of dust-suppressing foam and its effect on foam performance. *Process Saf. Environ. Prot.* **2019**, *123*, 351−357.
(9) Wang, H.; Wei, X.; Du, Y.; Wang, D. Effect of water-soluble polymers on the performance of dust-suppression foams: Wettability, surface viscosity and stability. *Colloids Surf., A* **2019**, *568*, 92−98.
(10) Colinet, J. F.; Rider, J. P.; Thimons, E. D. Controlling respirable dust in underground coal mines in the United States. 2006; *stacks.cdc.gov*.
(11) Raut-Jadhav, S.; Badve, M. P.; Pinjari, D. V.; Saini, D. R.; Sonawane, S. H.; Pandit, A. B. Treatment of the pesticide industry effluent using hydrodynamic cavitation and its combination with process intensifying additives (H2O2 and ozone). *Chem. Eng. J.* **2016**, *295*, 326−335.
(12) Long, X.; Zhang, J.; Wang, Q.; Xiao, L.; Xu, M.; Lyu, Q.; Ji, B. Experimental investigation on the performance of jet pump cavitation reactor at different area ratios. *Exp. Therm. Fluid Sci.* **2016**, *78*, 309−321.
(13) Lu, X.; Wang, D.; Shen, W.; Cao, K. A New Design of Double-Stage Parallel Adding Equipment Used for Dust Suppression in Underground Coal Mines. *Arabian J. Sci. Eng.* **2014**, *39* (11), 8319−8330.
(14) Wang, H.; Wang, D.; Lu, X.; Gao, Q.; Ren, W.; Zhang, Y. Experimental investigations on the performance of a new design of foaming agent adding device used for dust control in underground coal mines. *J. Loss Prev. Process Ind.* **2012**, *25* (6), 1075−1084.
(15) Zhu, X.; Wang, H.; Wang, D.; Xu, C.; Zhou, W.; Zhu, Y. Improved foam application at the tunnel face with large ventilation volume and low pressure supplied water. *Tunnelling and Underground Space Technology* **2020**, *95*, 103139.
(16) Lu, X.-x.; Wang, D.-m.; Zhu, C.-b.; Shen, W.; Zhong, X.-x.; Xu, C.-h. A new adding method of foaming agent used for foam dust suppression in underground coal mines. *J. Cent. South Univ.* **2015**, *22* (8), 3116−3122.
(17) Lu, X.; Wang, D.; Shen, W.; Zhu, C. Experimental investigation of the propagation characteristics of an interface wave in a jet pump under cavitation condition. *Exp. Therm. Fluid Sci.* **2015**, *63*, 74−83.
(18) Zhu, X.; Wang, D.; Wang, H.; Zhu, Y.; Xu, C. A cavitating device for mini quantitative liquid addition. *Flow Meas. Instrum.* **2017**, *57*, 87−93.
(19) Lu, X.; Wang, D.; Shen, W.; Zhu, C.; Qi, G. Experimental investigation on liquid absorption of jet pump under operating limits. *Vacuum* **2015**, *114*, 33−40.
(20) Long, X.; Zhang, J.; Wang, Q.; Xiao, L.; Xu, M.; Lyu, Q.; Ji, B. Experimental investigation on the performance of jet pump cavitation reactor at different area ratios. *Exp. Therm. Fluid Sci.* **2016**, *78*, 309−321.
(21) Abdulaziz, A. M. Performance and image analysis of a cavitating process in a small type venturi. *Exp. Therm. Fluid Sci.* **2014**, *53*, 40−48.
(22) Ulas, A. Passive flow control in liquid-propellant rocket engines with cavitating venturi. *Flow Meas. Instrum.* **2006**, *17* (2), 93−97.
(23) Ghassemi, H.; Fasih, H. F. Application of small size cavitating venturi as flow controller and flow meter. *Flow Meas. Instrum.* **2011**, *22* (5), 406−412.
(24) Zwart, P.; Andrew, G.; Thabet, B. A two-phase flow model for predicting cavitation dynamics. In *Fifth international conference on multiphase flow*; Yokohama, Japan, 2004; Vol. *152*.
(25) Yang, X.; Long, X.; Yao, X. Numerical investigation on the mixing process in a steam ejector with different nozzle structures. *Int. J. Therm. Sci.* **2012**, *56*, 95−106.
(26) Zhu, X.; Wang, D.; Xu, C.; Zhu, Y.; Zhou, W.; He, F. Structure influence on jet pump operating limits. *Chem. Eng. Sci.* **2018**, *192*, 143−160.
(27) Long, X. P.; Zeng, Q. L.; Yang, X. L.; Xiao, L. Structure optimization of an annular jet pump using design of experiment method and CFD. *IOP Conference Series: Earth and Environmental Science* **2012**, *15*, 052020.
(28) Bhusare, V. H.; Kalaga, D. V.; Dhiman, M. K.; Joshi, J. B.; Roy, S. Mixing in a co-current upflow bubble column reactors with and without internals. *Can. J. Chem. Eng.* **2018**, *96* (9), 1957−1971.
(29) Bhusare, V. H.; Dhiman, M. K.; Kalaga, D. V.; Roy, S.; Joshi, J. B. CFD simulations of a bubble column with and without internals by using OpenFOAM. *Chem. Eng. J.* **2017**, *317*, 157−174.
(30) Xiao, L.; Long, X.; Li, X.; Zeng, Q.; Yang, X. Numerical investigation on the recirculation in annular jet pumps. *J. Mech. Sci. Technol.* **2013**, *27* (6), 1603−1609.

https://doi.org/10.1021/acsomega.2c02814
ACS Omega 2022, 7, 29886−29900